Heavy Impurity Confinement in Hybrid Operation Scenario Plasmas with a Rotating 1/1 Continuous Mode

M. Raghunathan,[1] J. P. Graves,[1] T. Nicolas,[1] W. A. Cooper,[1] X. Garbet,[2] and D. Pfefferlé[3]
[1)] *École Polytechnique Fédérale de Lausanne (EPFL), Swiss Plasma Center (SPC), CH-1015 Lausanne, Switzerland.*
[2)] *CEA, IRFM, F-13108 Saint Paul-lez-Durance, France*
[3)] *Princeton Plasma Physics Laboratory, Princeton, New Jersey, USA*

(Dated: 10 August 2017)

In future tokamaks like ITER with tungsten walls, it is imperative to control tungsten accumulation in the core of operational plasmas, especially since tungsten accumulation can lead to radiative collapse and disruption. We investigate the behaviour of tungsten trace impurities in a JET-like hybrid-scenario with both axisymmetric and saturated 1/1 ideal helical-core in the presence of strong plasma rotation. For this purpose, we obtain the equilibria from `VMEC` and use `VENUS-LEVIS`, a guiding-centre orbit-following code, to follow heavy impurity particles. In this work, `VENUS-LEVIS` has been modified to account for strong plasma flows with associated neoclassical effects arising from such flows. We find that the combination of helical core and plasma rotation augments the standard neoclassical inward pinch compared to axisymmetry, and leads to a strong inward pinch of impurities towards the magnetic axis despite the strong outward diffusion provided by the centrifugal force, as frequently observed in experiments.

I. INTRODUCTION

In beam injected plasmas exhibiting strong toroidal flow, an important area of concern is the mitigation of confinement of heavy impurities. Unfortunately, beam injected experiments in JET and ASDEX upgrade, both with tungsten divertors, often exhibit rapid inward transport of tungsten impurities, leading to poor performance, and occasionally radiative collapse[1]. These poor plasma conditions can be mitigated by using auxiliary heating to peak the core temperature[2] shielding inward impurity transport, verified via fluid-based neoclassical[3] and turbulent gyrokinetic approaches[4]. Such techniques, however, have limited success during strong core MHD phenomena, such as neoclassical tearing modes (NTMs) and sawteeth[5], where the parallel transport associated with resistive islands is probably important. In JET, it has been stated that $n = 2, m = 3$ NTMs are now intolerable due to the massive influx of impurities associated with long-living core islands[6]. Scenario development is concerned with avoiding core magnetic islands.

The presence of strong toroidal flow leads to a significant modification particle confinement in the plasma. Because of their low thermal velocity, tungsten particles possess supersonic flow and are strongly trapped even in plasmas where the bulk-ion flow is strongly subsonic. In the axisymmetric limit, it has been shown that the centrifugal trapping leads to a strong enhancement of diffusivity[7,8]. One way to model the distribution of impurities is to follow the full 6D gyromotion of the impurity marker distribution (a so-called PIC approach) which is necessary when there are electric and magnetic field variation is of the order of the gyroradius of the particle. When such scale-length variations (including time-varying fluctuations[9]) are not present and the fields are smooth to the scale of the gyroradius, one may follow the guiding-centre orbits, which greatly reduces the computational cost. Proper accounting of centrifugal and neoclassical effects leads to the well-known impurity flux distribution[10] in axisymmetry, though little has been done so far using a PIC approach. Modelling attempts in the past have reproduced the strong diffusivity without reproducing the impurity peaking seen in experiments[11–13] essentially because the neoclassical transport arising from collisions of the trapped impurity particles with the passing particles background ions was neglected. This is the first area addressed by this manuscript, in which we follow a guiding-centre based PIC approach approach with a neoclassical collision operator.

In addition to plasma rotation and neoclassical effects, the presence of MHD modes can also have a significant effect on the particle orbits. In the current work, and in contrast to previous works involving resistive saturated structures associated with NTMs and sawteeth, we concentrate on plasma scenarios with $q > 1$ in the presence of a continuous $m = 1, n = 1$ 3D ideal MHD mode. In MAST and JET hybrid scenario experiments, where the q-profile has an extended region of low magnetic shear near the axis and stays above unity, experiments can exhibit long-lived continuous $n = 1$ helical structures[14,15]. These continuous modes, accompanied by toroidal rotation of the plasma and the mode, are surmised to be manifestations of a saturated and stable 1/1 internal kink. While 1/1 ideal internal kinks (without magnetic islands), degrade the confinement of fast ions[16], there is also increasing evidence of enhanced heavy impurity accumulation in the core region. We aim at a better understanding of the neoclassical impurity pinch (and other geometric effects) under such conditions in the plasma.

In order to compare impurity transport for kinked and unkinked magnetic fields with the neoclassical transport, turbulent transport is out of the scope of the current work. We use the 3D ideal MHD equilibrium code `VMEC`

to obtain our stationary 1/1 kinked magnetic fields[19,20]. One of the features of VMEC, is that one may obtain bifurcated solutions for an equilibrium with a helically distorted axis[21], which agrees with saturated initial value calculations of the internal kink mode[31]. This allows us to obtain accurate magnetic equilibria representing modes which are observed experimentally. Using the obtained equilibrium, one can use the guiding-center orbit-following PIC code VENUS-LEVIS[22] to observe the behaviour of different kinds of particles facing different equilibrium scenarios[16]. In addition, we have incorporated centrifugal and electric field effects in VENUS-LEVIS in the current work, allowing us to test particle behaviour under strong rotation. Furthermore, in order to develop an accurate model, it is of utmost importance to include neoclassical effects arising because of the collisions. We consider only the collisions between the impurity particles and the background ions[23,25], and neglect impurity self-collisions in the trace limit. In order to account for the discontinuity in the distribution function at the trapped-passing boundary of the background ions, we calculate the background ion parallel velocity analytically using established neoclassical theory[23,24]. The analytic computation of the parallel background velocity of the ions in axisymmetry is fairly simple. For cases in which a strong 3D deformation is present, we invert the continuity equation for computing the parallel flow velocity of the background ions. These calculations enable us, for the first time, to compute tungsten accumulation in realistic rotating hybrid plasma scenarios with continuous modes using a PIC approach.

The article is organized as follows. In Section II, we describe the complete implementation of the flows and neoclassical effects. In particular, in Section II, we explain the implementation of plasma rotation in the guiding-center code VENUS-LEVIS. As the collision operator responsible for the friction force requires an accurate description of the flows of the plasma background, we proceed to describe that in Section III. Then, we simulate the heavy impurity cases with VENUS-LEVIS for axisymmetry and helical core equilibria generated from VMEC in Section IV. In the end, we summarize our conclusions and future direction of work in Section V.

II. IMPURITY TRAJECTORIES WITH COLLISIONS

The orbits of the impurity particles are mainly influenced by two factors, i.e. plasma flow and collisions. Therefore, in this section, we aim to separate phenomenologically the effects of flow and collisions and explain their respective treatment in the codes we use. We begin by denoting the total flow of the species j to be $\mathbf{U}_j$, with the parallel and perpendicular components being $\mathbf{U}_{\parallel,j}$ and $\mathbf{U}_{\perp,j}$ respectively. The perpendicular flows for species j are given by

$$\mathbf{U}_{\perp,j} = \mathbf{U}_{0\perp,j} + \mathbf{U}_{1\perp,j}, \tag{1}$$

where the the flows $\mathbf{U}_{0,j}$ and $\mathbf{U}_{1,j}$, is given by

$$\mathbf{U}_{0\perp,j} = \frac{\mathbf{E}_0 \times \mathbf{B}}{B^2} \tag{2}$$

$$\mathbf{U}_{1\perp,j} = \frac{\mathbf{B} \times \nabla p_j}{n_j Z_j e B^2} + \frac{\mathbf{E}_1 \times \mathbf{B}}{B^2}. \tag{3}$$

The ordering of these flows and their parallel and perpendicular components, is associated with a Larmor-radius ordering for the background ion species, and Mach number ordering for the impurity species as applied in the guiding-centre formulation[18]. For the impurity particles, which possess a Mach number $\mathcal{M}_{0,W} = U_{0,W}/V_{th,W}$ (where we define for species j, $\mathcal{M}^2_{0,j} = m_j\Omega^2R^2/2T_j$) much higher than the background ions due to their low thermal velocity, the first term of Eq. 1 is much higher than the second term in the trace limit. The $\mathbf{E}_0 \times \mathbf{B}$ flow and the associated parallel flow $\mathbf{U}_{0\parallel,j}$ is established by the NBI beams, we assume that the total ensemble flow is purely toroidal. Imposition of a toroidal leading-order flow leads to simplifications in the computation of the associated centrifugal and Coriolis terms in the guiding-center formulation, and in the computation of the higher-order quasi-neutrality-preserving Φ_1, which leads to an associated $\mathbf{E}_1 \times \mathbf{B}$ flow. Furthermore, the leading-order ensemble flow is the same for every species, and therefore does not contribute to neoclassical effects. However, the parallel flows associated to pressure gradients are different for each species. As will be made clear, the higher-order parallel velocities $U_{1\parallel,j}$ are crucial for the neoclassical dynamics. The parallel flows are of the order of the perpendicular diamagnetic flow velocity, which is defined as

$$\mathbf{U}_{1\perp,j} - \frac{\mathbf{E}_1 \times \mathbf{B}}{B^2} = \frac{\mathbf{B} \times \nabla p_j}{n_j Z_j e B^2}. \tag{4}$$

Solving for $U_{1\parallel,j}$ exploits incompressibility for each plasma species, which at plasma equilibrium requires that $\nabla.\mathbf{U}_{1,j} = 0$. Once this parallel flow is computed, it must also be implemented in the collision operator from where the neoclassical effects arise. Thus, the particle velocity has to be provided to the collision operator such that it is in the frame of the background parallel flow $\mathbf{U}_{0,j} + \mathbf{U}_{1,j}$. This effectively means that the collision operator takes into account the difference between the particle parallel velocity and the background ion parallel velocity, thus providing neoclassical effects. We proceed to describe the calculation of neoclassical effects and the implementation of guiding-centre orbits in VENUS-LEVIS in the next two subsections.

A. Collisions and Inclusion of Neoclassical Effects

We proceed to describe the inclusion of neoclassical effects in this section, assuming the trace impurity limit (where impurity self collisions are neglected). As we know from well-established literature in neoclassical

physics of plasmas, the neoclassical transport of impurity particles is primarily caused by the collisional interaction of trapped impurity particles with passing particles of the thermal background[25]. The passing particles of a species cause a discontinuity in the distribution function because of the net parallel momentum they carry, and then the collisions between the passing and trapped particles aim to regularize this discontinuity.

In the trace impurity density limit, the collisions with the background ion species is the dominant mechanism and we can ignore the impurity self collisions. The background passing ions have a net parallel flow, which consists of two components, the first being the leading order flow $\mathbf{U}_{0\parallel,i}$ established by NBI and the second being the higher-order parallel flow $\mathbf{U}_{1\parallel,i}$ arising from pressure gradients in the plasma, as per the guiding-centre ordering. Since the impurity ions are shifted by the common flow $\mathbf{U}_0$, we only require the higher order parallel flow $U_{1\parallel,i}$ of the background ions in order to establish friction between the impurities and the background ions. The parallel flow $U_{1\parallel,i}$ can be obtained from the solution of the continuity equation $\nabla.\mathbf{U_{1,i}} = 0$. Moving to a frame where the higher-order electrif field $\mathbf{E}_1$ vanishes ($\mathbf{E}_1$ is treated later in the guiding-centre equations defined later), the general solution for $U_{1\parallel,i}$ from the continuity equation is given by[24]

$$U_{1\parallel,i} = -\left(\frac{g_2}{B} - \frac{B}{\langle B^2\rangle}\langle g_2\rangle\right)\frac{p_i'}{Z_i e n_i} + \frac{B}{\langle B^2\rangle}\langle U_{1\parallel,i}B\rangle \quad (5)$$

where g_2 is determined by

$$\mathbf{B}.\nabla\left(\frac{g_2}{B^2}\right) = \mathbf{B}\times\nabla\psi.\nabla\left(\frac{1}{B^2}\right) \quad (6)$$

$$g_2(B_{max}) = 0, \quad (7)$$

and $\langle f\rangle$ is the flux-surface average of the quantity f. The $\langle U_{1\parallel,i}B\rangle$ term in the expression is a constant of integration, and is chosen to be the parallel flow of the background ions computed from the neoclassical effects on the background ion species itself. Note that we neglect the higher-order electric field effects on the background plasma. Eq. (6) can be solved in straight-field line coordinates with a Fourier-transform, which reduces the parallel gradients to simple coefficients to the fourier transformed $\tilde{g}_2$, which then can be rearranged to inverse fourier transform back to g_2 with the boundary condition $g_2(B_{max}) = 0$.

To complete the solution of the parallel flow, a prescription for the parallel flow velocity in 3D magnetic fields can be obtained through the Shaing-Callen neoclassical model[23] in the appropriate regimes. We assume that both the impurities and background ions are in the high-collisionality Pfirsch-Schlüter regime. The expression for the common parallel flow in the Pfirsch-Schlüter regime is given by

$$\langle U_{1\parallel,i}B\rangle = -G_{PS}(\psi)\frac{T_i}{Z_i e}\left(\frac{p_i'}{p_i} + \frac{\mu_{2i}}{\mu_{1i}}\frac{T_i'}{T_i}\right) \quad (8)$$

where $G_{PS}(\psi)$ is a geometrical factor in the Pfirsch-Schlüter regime[32,33,49,50]

$$G_{PS}(\psi) = \langle g_2\rangle - \frac{\langle B^2\rangle}{\langle(\hat{b}.\nabla B)^2\rangle}\left\langle\frac{(\hat{b}.\nabla B)(\hat{b}.\nabla g_2)}{B^2}\right\rangle, \quad (9)$$

where $\hat{b} = \mathbf{B}/B$, a normalized unit vector in the direction of the magnetic field. In our current study, we ignore screening effects caused by temperature gradients by choosing a flat temperature profile in order to simulate the most pessimistic case of impurity accumulation.

By substituting Eqs. (8) and (9) in Eq. (5), the parallel velocity of the background ions is completely determined. The set of equations are fairly straightforward to solve in straight-field line coordinate systems. Before proceeding to the next section it is pointed out that the collision operator in `VENUS-LEVIS` is a Monte-Carlo operator taking the energy and pitch angle of the particle as the input. The colliding particle undergoes a random deviation of its pitch-angle λ and energy E, assuming the target distribution (in this case the background ion distribution) to be Maxwellian. In practice, the energy and pitch angle of the particle are computed in the frame of the ions moving with velocity $\mathbf{U}_{0,i} + \mathbf{U}_{1,i}$, with $\mathbf{U}_{1,i}$ given by Eq. (5), and fed to the Monte-Carlo operator. After transforming back to the rotating frame at $\mathbf{U}_{0,i}$, the post collision velocity can be computed. This effectively simulates the friction force between the impurities and the background ions. Benchmarking of the Monte-Carlo collision operator has already been done in `VENUS-LEVIS`[22]. It will be seen that the friction associated with $U_{1\parallel,i}$ causes impurity density peaking of the form $n_W \sim n_i^{Z_W}$ for the case of axisymmetry, which will be used to benchmark the collisional effects.

This completes the general description of the parallel flow $\mathbf{U}_{1,i}$ for the background ions. In the following section, we describe the implementation of the drifts associated with the leading-order flow $\mathbf{U}_{0,j}$.

B. Development and Implementation of the Guiding-Centre formulation with Rotation

In order for us to be able to evolve accurate particle trajectories for tungsten particles with flow, we must have an orbit-solver which allows for drifts produced by toroidal rotation. For this reason, we follow the guiding-center prescription suggested by Ref. 18, decomposing the particle guiding center velocity $\mathbf{V}_{gc}$ into flow and thermal components in the following manner:

$$\mathbf{V}_{gc,j} = \mathbf{U}_{0,j} + \mathbf{w}_j, \quad (10)$$

where $\mathbf{U}_{0,j}$ is the total leading-order ensemble flow velocity of the particle, and $\mathbf{w}_j$ is the thermal component of the velocity of the particle of species j. The advantage of the formulation in Ref. 18, over guiding-center formulations which explicitly solve for the orbits in the

rotating frame[30] is that this formulation allows us to incorporate a shear in the flow profile, which is essential for modelling cases which correspond closely to actual experimental conditions. In the current work however, we do not apply a sheared flow. Most importantly, the collisions which come through a collision operator need to be in the rest frame. Another advantage of this velocity decomposition is that the collisions can be directly imposed on the thermal part of the velocities, which are, by definition, in the rest frame of the plasma. Furthermore, the parallel and perpendicular dynamics can be resolved by further splitting the species flow and the thermal velocity into its parallel ($U_{0\parallel,j}, w_{\parallel,j}$) and perpendicular ($\mathbf{U}_{0\perp,j}, \mathbf{w}_{\perp,j}$) components. This ensures that the effective gyroradius $\rho_{\perp,jj}w_{\perp}/Z_jeB$ is much smaller than the scale-length of the field variation, thus within the guiding-centre approximations[22]. (For a JET-like system, the Larmor radius of tungsten impurities is a fraction of that of the thermal ions.)

The independent phase-space variables are chosen to be $(\mathbf{X}, \rho_{\parallel,j}, \mu_j)$, where $\mathbf{X}$ is the guiding-center position, $\mu = mw_{\perp,j}^2/2B$ is the magnetic moment, and $\rho_{\parallel,j}$, the parallel gyroradius is defined as

$$\rho_{\parallel,j} = \frac{m_j}{Z_je}\frac{w_{\parallel,j}}{B}. \tag{11}$$

The redefinition of the parallel variable in terms of $\rho_{\parallel,j}$ instead of $w_{\parallel,j}$ makes the guiding-centre derivation more convenient. The particle charge normalized Hamiltonian and Lagrangian are given by

$$\frac{\mathcal{H}_{gc}}{Z_je} = h = \Phi + \frac{\mu}{Z_je}B + \frac{1}{2}\frac{m_j}{Z_je}\left(\mathbf{U}_{0,j} + \frac{Z_je}{m_j}\rho_{\parallel,j}\mathbf{B}\right)^2, \tag{12}$$

and

$$\frac{\mathcal{L}_{gc}}{q} = l = \mathbf{A}^*.\dot{\mathbf{X}} - h, \tag{13}$$

where we define a modified vector potential $\mathbf{A}^*$ as

$$\mathbf{A}^* = \mathbf{A} + \frac{m_j}{Z_je}\mathbf{U}_{0,j} + \rho_{\parallel,j}\mathbf{B}. \tag{14}$$

The thermal corrections are supplied by the terms dependent on $\rho_{\parallel,j}$ and the centrifugal corrections are provided by the terms dependent on $\mathbf{U}_{0,j}$. This leads to the definition of a modified magnetic field $\mathbf{B}^*$

$$\mathbf{B}^* = \nabla\times\mathbf{A}^* = \mathbf{B} + \rho_{\parallel,j}\nabla\times\mathbf{B} + \frac{m_j}{Z_je}\nabla\times\mathbf{U}_{0,j}. \tag{15}$$

One can obtain the canonical equations of motion through the formal solution of the minimization of the variation of the Hamiltonian[18,41,44]. The final expression is

$$\dot{z^\alpha} = [\Omega^{-1}]^{\alpha\beta}(\partial_\beta h + \partial_t A^*_\beta), \tag{16}$$

where (α, β) can be any of the independent phase-space variables $(\mathbf{X}_j, \rho_{\parallel,j}, \mu_j)$. The Lagrange bracket $\Omega_{\alpha\beta}$ is defined to be

$$\Omega_{\alpha\beta} = \partial_\alpha A^*_\beta - \partial_\beta A^*_\alpha. \tag{17}$$

The Lagrange bracket can be shown to be

$$\Omega_{\alpha\beta} = \begin{pmatrix} 0 & B_q \\ -B_p & \sqrt{g}B^{*r}\epsilon_{rpq}\end{pmatrix}, \tag{18}$$

where (p, q, r) are the components of $\mathbf{X}$ and ϵ is the Levi-Civita symbol. Consequently its inverse

$$[\Omega^{-1}]^{\alpha\beta} = \frac{1}{B_pB^{*p}}\begin{pmatrix} 0 & -B^{*q} \\ B^{*q} & \frac{B_r}{\sqrt{g}}\epsilon^{rpq}\end{pmatrix}. \tag{19}$$

From Eq. (16)-(19), we get

$$\partial_{\rho_{\parallel,j}}h = U_{0\parallel,j}B + \frac{Z_je}{m_j}\rho_{\parallel,j}B^2 \tag{20}$$

and

$$\partial_p h = -E^*_p = -E_p + \left(\frac{\mu}{Z_je} + \frac{Z_je}{m_j}\rho^2_{\parallel,j}B\right)\partial_p B + \frac{m_j}{Z_je}\partial_p(U^2_{0,j}) + \rho_{\parallel,j}\partial_p(U_{0\parallel,j}B), \tag{21}$$

respectively, where E^*_i is the electric field with thermal and centrifugal corrections. The modified electric field $\mathbf{E}^*$ can be written in vector form as

$$\mathbf{E}^* = \mathbf{E} - \left(\frac{\mu}{Z_je} + \frac{Z_je}{m_j}\rho^2_{\parallel,j}B\right)\nabla B - \frac{1}{2}\frac{m_j}{Z_je}\nabla(U^2_{0,j}) - \rho_{\parallel,j}\nabla(\mathbf{U}_{0,j}.\mathbf{B}), \tag{22}$$

where $\mathbf{E} = -\nabla\Phi_0 - \nabla\Phi_1$. Φ_0 is the electric potential responsible for driving the toroidal flow, and Φ_1 is the higher-order centrifugal correction as explained shortly below. The equations of motion are obtained by substituting equations (19)-(20) in equation (16),

$$\begin{pmatrix} \dot{\rho_{\parallel,j}} \\ \dot{X^p_j}\end{pmatrix} = \frac{1}{B_pB^{*p}}\begin{pmatrix} 0 & -B^{*q} \\ B^{*q} & \frac{B_r}{\sqrt{g}}\epsilon^{rpq}\end{pmatrix}\begin{pmatrix} U_{0\parallel,j}B + \frac{Z_je}{m_j}\rho_{\parallel,j}B^2 \\ -E^*_q\end{pmatrix}. \tag{23}$$

Finally, the relevant guiding-center equations are

$$\dot{\rho_{\parallel,j}} = \frac{B^{*q}E^*_q}{B_pB^{*p}} = \frac{\mathbf{E}^*.\mathbf{B}^*}{\mathbf{B}.\mathbf{B}^*} \tag{24}$$

$$\dot{X^p_j} = \left(U_{0\parallel,j} + \frac{Z_je}{m_j}\rho_{\parallel,j}B\right)\frac{BB^{*p}}{B_pB^{*p}} + \frac{\epsilon^{pqr}}{\sqrt{g}}\frac{B_rE^*_q}{B_pB^{*p}} = \left[\left(U_{0\parallel,j} + \frac{Z_je}{m_j}\rho_{\parallel,j}B\right)\frac{B\mathbf{B}^*}{\mathbf{B}.\mathbf{B}^*} + \frac{\mathbf{E}^*\times\mathbf{B}}{\mathbf{B}.\mathbf{B}^*}\right]^p. \tag{25}$$

Using the ideal Ohm's law, the expressions for $\dot{\rho}_{\parallel,j}$ and $\dot{\mathbf{X}}_j$ can also be written in the form

$$\dot{\rho}_{\parallel,j} = \frac{\mathbf{B}^*}{\mathbf{B}.\mathbf{B}^*}.\left\{\nabla\Phi_1 + \frac{\mu_j}{Z_je}\nabla B + \frac{m_j}{Z_je}\mathbf{U}^*_{0,j}.\nabla\mathbf{U}^*_{0,j}\right\} \tag{26}$$

$$\dot{\mathbf{X}}_j = \mathbf{U}^*_{0,j} + \frac{\mathbf{B}}{\mathbf{B}.\mathbf{B}^*} \times \left\{ \nabla\Phi_1 + \frac{\mu_j}{Z_j e}\nabla B + \frac{m_j}{Z_j e}\mathbf{U}^*_{0,j}.\nabla\mathbf{U}^*_{0,j} \right\} \tag{27}$$

as can be seen in Appendices A, where $\mathbf{U}^*_{0,j} = \mathbf{U}_{0,j} + Z_j e/m_j \rho_{\parallel,j}\mathbf{B}$. The centrifugal and Coriolis forces arise from the last term on the RHS of the above expression (See similar comments in Ref. 18). We can see that the effects of plasma rotation are now incorporated in the guiding-center equations.

The most general solution to $\mathbf{U}_{0,j}$ is obtained by inverting the continuity equation $\nabla.\mathbf{U}_{0,j} = 0$ and can be written, assuming the lowest order electric potential Φ_0 is a flux-surface function, in the Pfirsch-Schlüter regime[32] as

$$\mathbf{U}_{0,i} = \left\{ -\left(\frac{g_2}{B} - \frac{B}{\langle B^2 \rangle}\langle g_2 \rangle \right) - \frac{B}{\langle B^2 \rangle} G_{PS} + \frac{U_{0\parallel,i,bc}}{B} \right\} \Phi_0' \mathbf{b} + \frac{\mathbf{B} \times \nabla\psi}{B^2}\Phi_0', \tag{28}$$

where $U_{0\parallel,i,bc}$ is the boundary condition. Note that $U_{0\parallel,i,bc}$ is zero in the case of axisymmetric magnetic fields[32]. In this work, we choose a value of $U_{0\parallel,i,bc}$ to impose a purely toroidal flow. The leading-order flow is then imposed as

$$\mathbf{U_0} = U_{\phi 0,j}\nabla\phi = \Omega(\psi)R^2\nabla\phi, \tag{29}$$

where $\Omega(\psi)$ is the angular velocity. This makes the computations of gradients of the flow in Eq. (27) much simpler as elaborated in Appendix B. It is important to note that the leading-order flow in its most general form is not purely toroidal, but actually lies along the intersection of the contours of ψ and B[26]. The treatment of a complex flow of such nature is out of the scope of the current article, and will be a subject of investigation in future works.

As mentioned earlier, because of the toroidal flow, the centrifugal effects come into play on the particle orbits. The centrifugal forces are mass sensitive and hence act on the ions and electrons to different extents. This leads to a charge separation which threatens to break the quasi-neutrality of the plasma. In reality, a compensating electric field comes into play to prevent the violation of quasi-neutrality. We denote this compensating potential as Φ_1 (and its corresponding electric field $\mathbf{E}_1$) which is less than the leading-order potential in the guiding center formulation. As derived in Appendix C, the quasi-neutrality correcting potential takes the following form in axisymmetry

$$\Phi_1 = \frac{T_e}{T_i + T_e}\frac{m_i}{2e}\Omega^2 R^2. \tag{30}$$

We mention that we impose the axisymmetric form of Φ_1 for the simulations with 3D fields as well, as the preservation of quasi-neutrality and its associated potential in a 3D rotating MHD equilibrium is still an open question.

Additionally, in inductively-driven plasmas, there is also a loop voltage V_{loop} induced electric field $E_{\parallel,loop}$. The parallel electric field is responsible for driving the plasma current results in an inward pinch of particles, known as the Ware pinch[36]. It leads to a usually very small inward velocity for the heavy impurities, which has been established to not play a significant role in heavy impurity confinement in the presence of strong plasma rotation[12]. With high temperatures and low loop-voltages in JET and high $\mathcal{M}^2_{0,W}$ flows for tungsten particles, this pinch will not be a significant effect to consider. This parallel electric field is very low (V_{loop} is of the order of 0.1V) for a JET pulse during the NBI-driven phase of the pulse and does not play a significant role when strong rotation is involved. Having derived the guiding-center formulation and its accompanying perpendicular drifts, we move on to compute the equilibria and the neoclassical quantities associated with the geometry of the axisymmetric and 3D equilibria.

III. NEOCLASSICAL PROPERTIES OF AXISYMMETRIC AND HELICAL-CORE EQUILIBRIA

The ideal MHD equilibria, both axisymmetric and those possessing a saturated 1/1 internal kink, are generated for a JET-like case with the Variational Moments Equilibrium Code (VMEC)[19,20]. `VMEC` generates equilibria using the steepest descent method minimizing the ideal MHD energy functional:

$$\mu_0 W = \int\int\int d^3x \left(\frac{B^2}{2} + \frac{\mu_0 p(s)}{\Gamma - 1} \right). \tag{31}$$

For axisymmetry, the minimization of Eq. 31 is functionally equivalent to arriving at an equilibrium by solving the Grad-Shafranov equation under the appropriate boundary conditions. For obtaining a 3D saturated 1/1 internal kink, one specifies a skewed axis with an appropriate q-profile that can effectively converge upon a saturated helical core. The flow is imposed later in the guiding-centre equations to study particle behaviour. The helical core equilibrium with $q_{min} \gtrsim 1$ has been shown to correspond to the stable 1/1 internal kink mode in hybrid scenarios[31]. The reason for ignoring the rotation in calculation of the equilibrium fields is that currently there is no consistent MHD model for rotation in 3D plasmas. In the limit where the bulk ions are strongly subsonic, inertial effects due to the centrifugal force are negligible, and as such we may assume that the plasma rotates toroidally in a 3D kinked plasma just as it does to leading order for an axisymmetric plasma. Indeed the Mach number for bulk ions is such that the bulk flow is strongly subsonic, and hence any empirically observed MHD non-axisymmetry would move past magnetic probes with an associated frequency $n\Omega$, where n is the toroidal mode number, and Ω is the toroidal plasma rotation frequency. The dominant MHD mode in the current work is a saturated $n = 1, m = 1$ continuous mode.

We proceed to generate the required magnetic equilibria. We choose appropriate pressure and q-profiles for

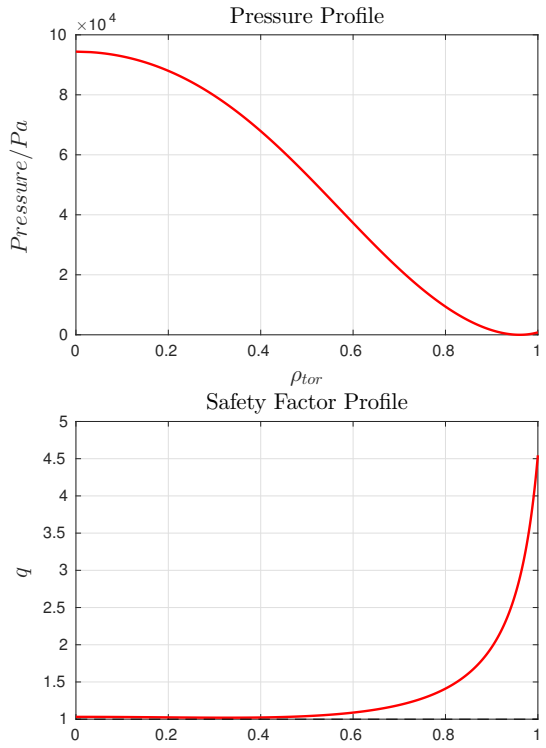

FIG. 1. The selected profiles used for generating the helical and axisymmetric branches of the VMEC equilibria.

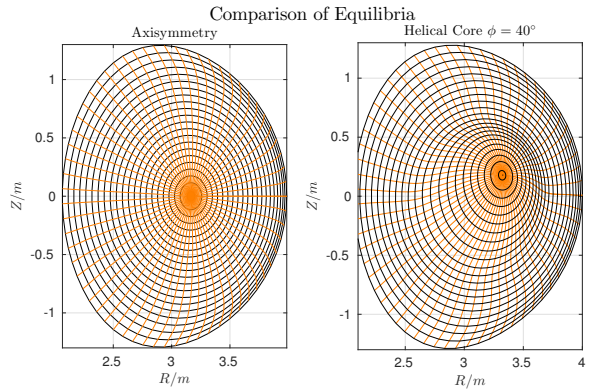

FIG. 2. Toroidal cuts of the VMEC equilibria for a helical core and its axisymmetric sister state. Notice how the constant pressure surfaces are shifted by the saturated internal kink.

the equilibria as seen in Fig. 1, and create a helical core equilibrium by initially prescribing an appropriate helical displacement of the magnetic axis ($\sim 0.2m$ helical skew in the radial direction). On constraining the number of toroidal modes to zero, we obtain an axisymmetric bifurcated solution. The comparison of the axisymmetric and helical core sister states can be seen in Fig. 2. The equilibria are low current hybrid scenario equilibria, with a normalized beta value of $\beta_N = 3.1\%$, as seen in Tab. I. We use these equilibria as the basis for our electric and magnetic fields in the guiding-centre orbits.

TABLE I. Values of essential parameters used in the equilibrium generation for a JET-like case

Toroidal Current I_p	1.79MA
On axis pressure P_0	1.0×10^5Pa
On axis temperature T_0	2.1keV
Safety factors q_0, q_{95}	$1.053, 4.683$
Edge poloidal flux Φ_{edge}	8.27Wb
On axis field B_0	2.88T
Major and minor radii R_0, a	3.238m, 1.14m
Helical skew δ_h	0.23
Beta values β, β_N	$2.56\%, 3.16\%$
Grid Sizes (n_s, n_θ, n_ϕ)	$(231, 45, 25)$
Mode numbers (m, n)	$(9, 5)$

We use the equilibrium to compute the parallel velocity $U_{1\parallel,i}$ for the background equilibria. It is fairly difficult to invert the continuity equation assuming VMEC-coordinates. Conversion to straight-field line coordinate system such as Boozer coordinates[17] makes the calculation for the parallel velocity much easier. This is accomplished using `TERPSICHORE`[51], a code package that also allows for a convenient mode selection so as to ensure a precise conversion of the VMEC mode spectrum into the Boozer mode spectrum. Furthermore, after having converted the magnetic equilibrium into Boozer coordinates, we integrate equation 6 by transforming them into Fourier-space of the Boozer spectrum, where the gradients are represented as simple scalars in the direction of the magnetic field. However, this leads to the problem of numerical resonances at rational q-surfaces[38]. These spikes occur due to the parallel gradient operator $\mathbf{B}.\nabla$ being proportional to $(m\Psi' - n\Phi')^{-1}$, which is singular at rational $q = m/n$ surfaces in Fourier space. The mitigation of these numerical resonances is performed by inclusion of a resonance detuning operator Δ_{mn}, which numerically smooths over the singularities. The resonance detuning operator is defined as the following

$$\Delta_{mn} = \Delta\left[(m+1)\Psi' - n\Phi'\right] \tag{32}$$

where Δ is a dimensionless factor that determines the amplitude of the numerical smoothing. The singularities are avoided by changing the denominator of the following to a non-zero value

$$\frac{1}{m\Psi' - n\Phi'} \to \frac{m\Psi' - n\Phi'}{(m\Psi' - n\Phi')^2 + \Delta_{mn}^2}. \tag{33}$$

It is important to notice that the resonance detuning scheme is just a numerical tool to smooth over the singularities on the resonant $q = m/n$ surfaces. In reality, these resonances are equivalent to parallel current sheets which, with finite resistivity, would be replaced by islands and local pressure flattening. However, such physics cannot be accounted for by an ideal MHD equilibrium code like VMEC. The spikes diminish as the value of Δ increases. Crucially, quantities in the helically-deformed

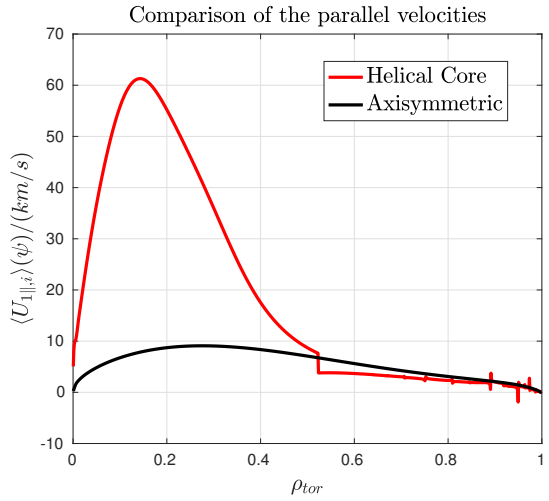

FIG. 3. The computed values of the parallel velocity $U_{1\|,i}$.

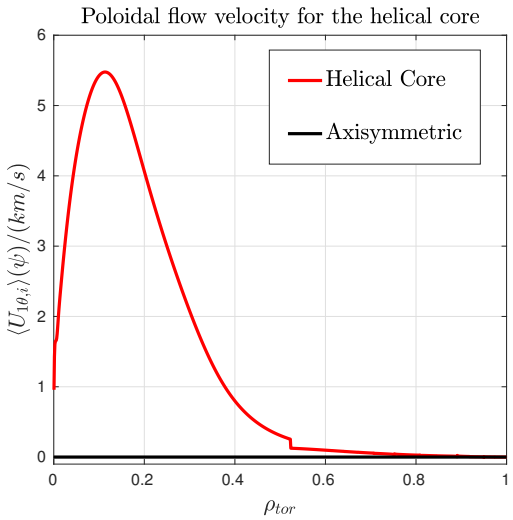

FIG. 4. The associated value of the poloidal flow velocity $U_{1\theta,i}$ for the helical core.

region are unaffected by the value of Δ. As will be seen, the 1/1 non-resonant internal kink mode is a particularly interesting application because the core 3D structure avoids resonance, hence is independent of the details of the resonance detuning parameter, and largely the physics of resistivity, should it have been included.

As explained in the previous section, it is of interest to compute the surface-averaged parallel velocity, i.e. the surface average of Eq. 8, $\langle U_{1\|,i}\rangle$ for axisymmetric and helical cores in the Pfirsch-Schlüter regime. This gives us an insight into how the helical distortion modifies the parallel velocities, $\langle U_{1\|,i}\rangle$, which are shown in Fig. 3. It is worth noting that, for the 3D equilibrium, this leads to a finite poloidal flow, as seen in Fig. 4, whereas it is zero for the axisymmetric case in the Pfirsch-Schlüter regime as is well-known neoclassical literature in the limit of zero temperature gradients[23,25]. This will become important to interpret the simulation results, as will be seen.

We notice immediately that, for the 3D case, there is a strong augmentation of the parallel velocity $\langle U_{1\|,i}\rangle$ in the helical core region, as compared to axisymmetry, as observed in the previous work of the authors in Ref. 39. This increase in the helical core region is due to the parallel gradient operator being very small in the core $((m\Psi' - n\Psi')^{-1}$ being large) due to the near resonance of the 1/1 mode. The low value of $(m\Psi' - n\Psi')$ consequently causes the magnification of the geometrical factor in the helical core region. Similar enhancements to the bootstrap current due to the helical core have been reported earlier[39]. The enhanced parallel velocity $U_{1\|,i}$ is accompanied by the presence of a finite poloidal flow for the 3D case, whose importance will be explained later.

IV. SIMULATIONS OF TUNGSTEN NEOCLASSICAL TRANSPORT

In this section, we perform full-f simulations of tungsten species in the trace limit interacting with the background plasma through collisions. The particle trajectories are evolved by the guiding-centre formulation and the collisions with the background plasma are made by the Monte-Carlo collision operator described in the preceding section. The background fields are used from the `VMEC` equilibria also described in the previous section. The full distribution is initialized in terms of markers weighted appropriately to emulate the chosen initial distribution. The evolution of the distribution and the marker weights provides us the evolution of the distribution in time. For all our guiding-centre simulations, we choose a toroidal angular velocity $\Omega = 1.2 \times 10^5$rad/s (corresponding roughly to 20kHz and Mach number $\mathcal{M}_{0,W} = 8.94$) for the toroidal ensemble flow. We initialize a full distribution of heavy tungsten impurity with an effective charge of $Z_W = 40$ and an initial Maxwellian density of the form $n_W = n_i \times 10^{-4}$, such that the impurity contributions to the plasma and the fields can be neglected. We initialize 2^{15} particles weighted appropriately to emulate the full distribution and let the particles evolve their orbits until the density profile saturates. It is necessary to resolve very finely in time because of the large angular rotation speed, and we find that the precision of convergence of the simulations does not significantly increase beyond 2^{15} particles, and hence this choice of the number of the particles leads to adequate precision while optimizing on the computation times. The initial normalised pressure and temperature profiles are chosen to be the same as those of the background ions and electrons used for the `VMEC` equilibria as in Fig. 1. We assume a flat background ion and electron temperature profiles with $T_{0,i} = 2.1$keV, in

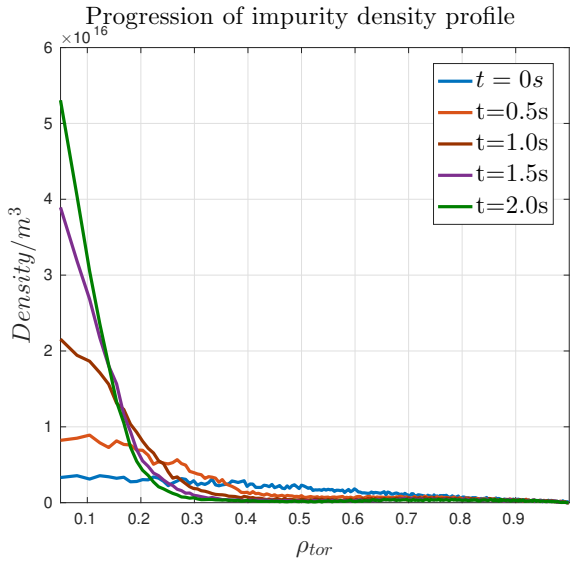

FIG. 5. The density profile of the impurity with time for an axisymmetric JET-like equilibrium without rotation. Notice the slow but constant inward drift of the density, leading to heavy impurity peaking on the axis.

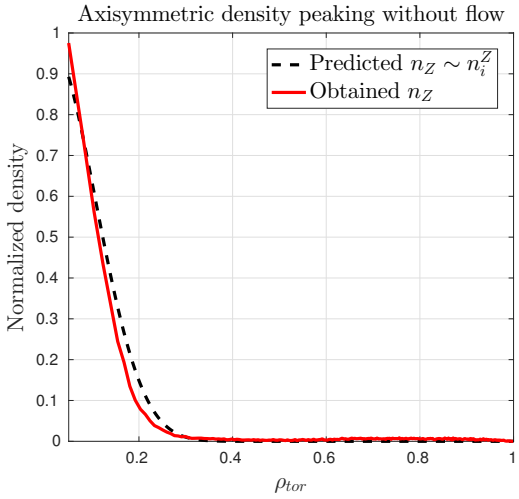

FIG. 6. Plot of the predicted and numerically obtained impurity density for an axisymmetric equilibrium without flow. The black dashed curve represents the one plotted from Eq. (34). We find that they are in good agreement.

order to choose the most pessimistic case of inward impurity pinch without the potentially beneficial screening provided by the thermal gradient.

A. Benchmark for Axisymmetry and Plasma Rotation

We first start with a benchmark to test whether the model has been implemented properly. In order to do so, we choose an axisymmetric equilibrium, initialise the particles as explained previously, and let the orbits evolve

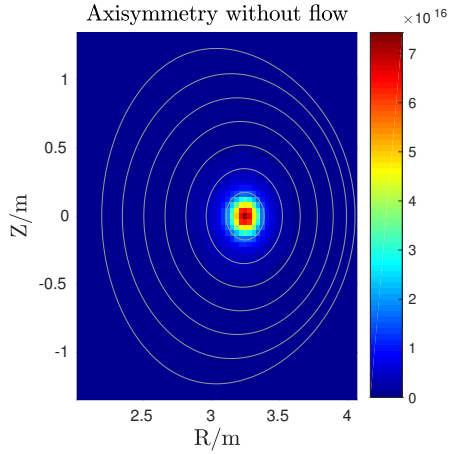

FIG. 7. Density plot for the axisymmetric equilibrium without flow at $t = 2s$. As we expect, the tungsten impurities concentrate on the axis with the density following the predicted density.

in the absence of flow, and let the density profile evolve to saturation. We notice that the density profiles take about $t \approx 2s$ to evolve to saturation. From the neoclassical theory of impurities without flow for axisymmetric conditions, we would expect the saturated density profile to be[25]

$$\frac{\langle n_W(r)\rangle}{\langle n_W(r=0)\rangle} = \left(\frac{n_i(r)}{n_i(r=0)}\right)^{Z_W/Z_i}, \qquad (34)$$

i.e. a very peaked density indicating that the particles have undergone a significant inward drift. During the progression of the simulation, we see from Fig. 5, that the particles are indeed drifting inwards with time, leading to density saturation at around $t = 2s$. Having established the inward drift of the particles, we can also observe from Fig. 6 that the final normalized density profile agrees reasonably well with the predicted normalized density. Additionally, the inward drift speed can be heuristically estimated to be in the order of 1m/s, which agrees with benchmarked values from studies performed previously[3]. Fig. 7 confirms that the density of the tungsten impurities over R and Z strongly peaks near the axis.

We now examine the effect of imposing a strong leading-order flow $\mathbf{U}_{0,i}$ on the heavy impurity particles. In Ref. 10 and 34, by assuming that the impurities have a strong poloidal asymmetry caused by the presence of the centrifugal force and the corrections for quasi-neutrality, the equations for parallel momentum balance and ambipolarity were solved to obtain the flux-surface averaged radial impurity flux $\langle \Gamma_W . \nabla r \rangle$

$$\langle \Gamma_W.\nabla r\rangle_\psi = -D_{PS}(1+\mathcal{M}_*^2)^2\langle n_W\rangle \times \left\{\partial_r \ln\langle n_W\rangle - \left(1-\frac{\mathcal{M}_*^2}{1+\mathcal{M}_*^2}\frac{Z_i e n_i}{p'}\langle U_{1,i\theta}\rangle\right)\frac{Z_W}{Z_i}\partial_r \ln p_i - \frac{\tilde{m}}{m_*}\left(\frac{\mathcal{M}_*^2(1+3\epsilon\mathcal{M}_*^2+2\epsilon\mathcal{M}_*^4) - R_0\partial_r\epsilon\mathcal{M}_*^2}{R_0\epsilon(1+\mathcal{M}_*^2)^2}\right)\right\}, \tag{35}$$

and where $\epsilon = r/R_0$ is the inverse aspect-ratio, $D_{PS} = 2\epsilon^2(T_i/Z_W e B_{\theta 0})^2$ is the stationary Pfirsch-Schlüter diffusion coefficient, and the angle brackets $\langle\rangle$ indicate surface-averaged quantities. The effective Mach number $\mathcal{M}_*^2$ (see Appendix C) is defined as

$$\mathcal{M}_*^2 = \mathcal{M}_{0,W}^2\left(1-\frac{m_i T_e}{m_W(T_i+T_e)}\right), \tag{36}$$

and the masses $\tilde{m}$ and m_* as

$$\tilde{m} = m_W - Z_W m_i, \text{and} \tag{37}$$

$$m_* = m_W - \frac{T_e}{(T_i+T_e)}m_i \tag{38}$$

respectively. $\langle U_{1,i\theta}\rangle$ is the surface-averaged poloidal component of $\mathbf{U}_{1,i}$ which can be expanded into

$$\langle U_{1,i\theta}\rangle = \left\langle \left\{\left(\frac{g_2}{B^2}-\frac{\langle g_2\rangle}{\langle B^2\rangle}\right)+\frac{G_{PS}(\psi)}{\langle B^2\rangle}\right\}\mathbf{B}.\nabla\theta + \frac{\mathbf{B}\times\nabla\psi.\nabla\theta}{B^2}\right\rangle \frac{p_i'}{Z_i e n_i}. \tag{39}$$

To understand Eq. (35), the physical contributions can be broken down term-by-term. The overall coefficient $D_{PS}(1+\mathcal{M}_*^2)^2$ implies that the convective and diffusive processes are enhanced by the centrifugal effects by a factor of the Mach number squared. This plasma rotation dependent enhancement of the impurity flux is related to the deep centrifugal trapping experienced by the heavy impurity particles. As trapped particles spend most of their time on their bounce-tips, the random walk step size is increased from their gyroradius to distance between their bounce tips, thus contributing to the increased diffusivity (as noticed later in the saturation times of the two cases with plasma flow.) The first term in the curly brackets proportional to $\partial_r \ln\langle n_W\rangle$, implies an outward flux contribution from the impurity density gradient, which remains small in the trace limit. The second term, proportional to $\partial_r \ln p_i$ is responsible for the inward flux of the particle, and is enhanced by presence of poloidal flow along with the toroidal flow. The averaged poloidal velocity remains approximately zero in the axisymmetric limit in the Pfirsch-Schlüter regime, as seen in Fig. 4, and hence does not effectively amplify the peaking in the axisymmetric limit. The third term consisting of an expression in terms of the effective Mach number $\mathcal{M}_*$, provides an outward flux as a result of centrifugal effects.

The steady state of impurities is reached when the net flux of impurities vanishes, that is $\langle \Gamma_W.\nabla r\rangle = 0$. On setting the RHS of the expression to zero, in the large aspect ratio limit with an unsheared $\mathcal{M}_*^2$, with $\langle U_{1\theta,i}\rangle \approx 0$ for axisymmetry, we arrive at a steady-state impurity density profile for unsheared flows as follows

$$\frac{\langle n_W(r)\rangle}{\langle n_W(0)\rangle} = \left(\frac{n_i(r)}{n_i(0)}\right)^{Z_W/Z_i} \times \exp\left\{\frac{\tilde{m}}{m_*}\frac{(3+2\mathcal{M}_*^2)\mathcal{M}_*^4}{(1+\mathcal{M}_*^2)^2}\frac{r}{R_0}\right\}. \tag{40}$$

It can be immediately seen that the density profile with flow does not peak on the axis, but is modulated by an flow-dependent exponential term moving the saturated density profile off-axis. We also recover Eq. 34 from the above expression by setting the Mach number $\mathcal{M}_* = 0$.

We now perform a full-f simulation with $20kHz$ flow for axisymmetry and we find that the particles do not make it all the way into the core region, and saturate at the edge of the core region, which can be seen in Fig. 8. Also, from the plot of the density on the toroidal plane, in Fig. 9, we notice that the particles are deeply trapped centrifugally, as expected, and settle off-axis. This is because of the competition between the inward pinch offered by the neoclassical effects and the outward drift because of the centrifugal effects in Eq. 35. In the expression for steady-state density, Eq. 40, we see that the centrifugal effects add an exponential term that competes against the density peaking and can lead to off-axis peak-

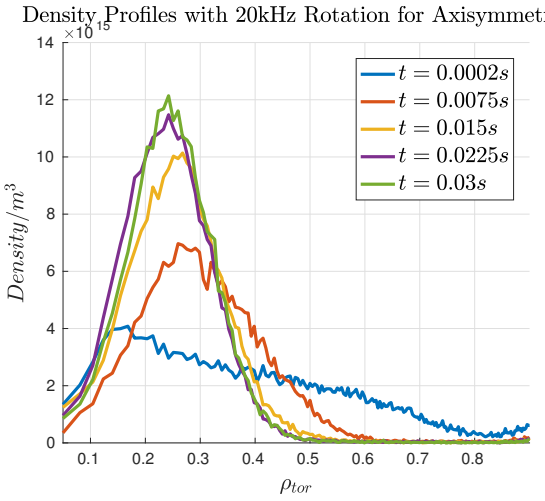

FIG. 8. The time progression of the density profile for an axisymmetric equilibrium case with 20kHz rotation.

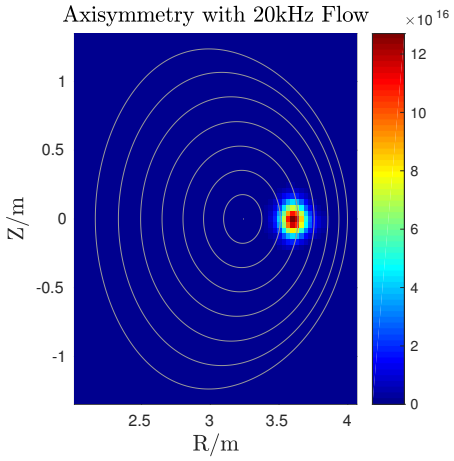

FIG. 9. Plots of density of tungsten for the axisymmetric equilibrium with 20kHz rotation. We notice that the impurities, deeply trapped on the low field side, saturate off-axis

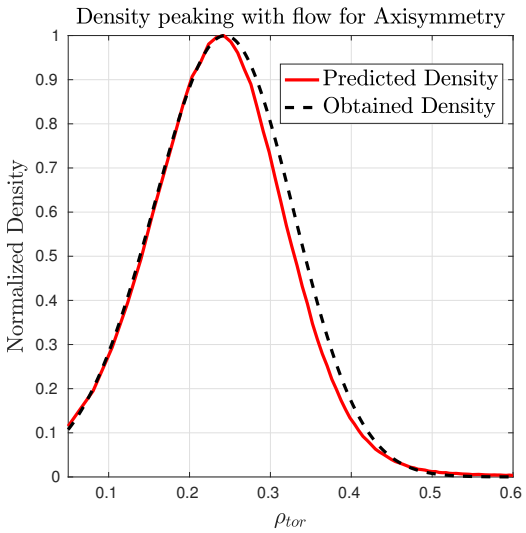

FIG. 10. Plot of the predicted and numerically obtained impurity density for an axisymmetric equilibrium with 20Khz plasma flow. The dashed black curve represents the saturated state obtained from Eq. (40). We find that they are in reasonable agreement, with the off-axis peaking reasonably predicted well.

ing. This is also consistent with our numerical calculation of the parallel velocity $U_{1\|,i}$, since outward centrifugal advection starts competing with the inward pinch when the parallel velocity of the background ions is low, and hence the impurities do not feel a strong inward pinch in the low q-shear core region. Using Eq. 40, we evaluate the local maximum of the density distribution, by setting the derivative to zero. We find the local maximum occurs at $r/a \approx 0.23$, which agrees reasonably with the maximum of the density in Fig. 8 . We also notice a reasonable agreement between the predicted surface-averaged density from Eq. 40 (setting $\mathcal{M}_*^2 \approx 80$) and our numerically obtained saturated surface-averaged density, which can be seen in Fig. 10.

Furthermore, if we impose a flow with non-zero Mach number $\mathcal{M}_*$ and remove neoclassical effects, i.e. set the coefficient of the term $\partial_r \ln p_i$ relating to background ions to zero, we find that the final density is effectively zero everywhere because of the dominant centrifugal advection term. In order to test this with our numerical scheme, we initialize the particles in the same manner as previously, but we impose a flow Ω of 1.2×10^5rad/s or 20kHz equivalently, and set the background parallel velocity to zero, i.e. $U_{1\|,i} = 0$, therefore imposing no neoclassical physics. On doing so, we find a strong outward drift accompanied by a quick loss of particles, with the particle numbers depleting to zero in a very short time. If we define the impurity confinement time as the time it takes for the density to drop to $1/e$ its initial value, the confinement time is of the order of 40ms, which agrees with the PIC simulations in Ref. 12, which were also performed without the inclusion of the neoclassical effects through collisions.

B. Simulations for a Helical Core Equilibrium

In the previous subsection we saw that with strong rotation the impurities do not peak on the magnetic axis if the plasma is axisymmetric, even when there is no temperature screening. However, experiments often show strong peaking on the axis even in the presence of strong flows[4]. This section investigates the possibility of axial neoclassical peaking due to 3D effects in the core despite the presence of centrifugal effects.

For our simulations, we use the parallel flow velocity in the Pfirsch-Schlüter regime as obtained in the previous section for the helical core equilibrium. The surface-averaged parallel velocity profile $\langle U_{1\|,i} \rangle$, as seen in the Fig. 3, is significantly different from that for the axisymmetric equilibrium. In particular, there is a significantly higher parallel flow for the background ions in the helical core than for the axisymmetric core. Therefore, we expect a different value of the neoclassical inward pinch for the impurity species for the helical core. We proceed to perform a full-f simulation for the helical core equilibrium rotating at 20kHz including neoclassical effects. We see, in Fig.11, that the particles have made their way into the core very near the magnetic axis, and we notice the saturation around $t \approx 0.015s$. Furthermore looking into the density distribution over various toroidal cuts, in Fig.12, we observe that the particles stay close to the axis, following the helical core. Thus, we find that there is a strong effect of the helical core amplitude on the inward pinch faced by impurity particles, arising implicitly through the associated neoclassical effects.

We again consider the analytical radial flux expression

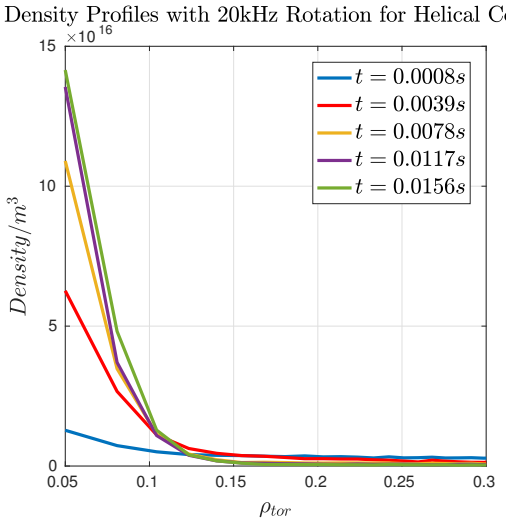

FIG. 11. The plots of the density profile for a helical core equilibrium with 20kHz rotation (zoomed in from $s = 0.05 - 0.3$).

for impurities Eq. 35. Strictly speaking, Eq. 35 is only valid for axisymmetry, however it contains an explicit dependence on the relation of the fluxes to the background ion poloidal flow $U_{1\theta,i}$, and therefore it is instructive to study the same expression using the background poloidal flow $U_{1\theta,i}$ obtained for the helical core to see its explicit effect on the saturation density peaking. Firstly, as we know from Eq. 35, toroidal rotation enhances the diffusivity by a factor of $(1+\mathcal{M}_*^2)^2$, which enhances the rate of peaking for plasma rotation. This enhanced diffusivity is in accordance with our observation of the saturation times of the peaked impurity density, reducing from about $t \sim 2s$ for the non-rotating case to $t \sim 15ms$ for 20kHz rotation. We notice from the second term on the RHS of Eq. 35 that the inward impurity flux gets further modulated by a factor of $\langle U_{1\theta,i}\rangle$, in addition to the centrifugal enhancement. This averaged poloidal velocity is a purely geometric effect, and scales in the same manner as the parallel velocity $U_{1\parallel,i}$, seen in Fig. 4. One can notice that $\langle U_{1\theta,i}\rangle \approx 0$ in the axisymmetric limit, as is expected from conventional neoclassical literature[23,25], but is enhanced by an order of magnitude for the helical core in the core region. Additionally, this geometrical enhancement only appears in the flux through a factor of $\mathcal{M}_*^2/(1+\mathcal{M}_*^2)$. If one neglects rotation, setting $\mathcal{M}_*^2 = 0$, we find the density peaking to scale identically for the axisymmetric and helical core cases, irrespective of the geometry, which we recover in Fig. 13. The saturated impurity density profile from Eq. 35 is as follows:

$$\frac{\langle n_W(r)\rangle}{\langle n_W(0)\rangle} = \left(\frac{n_i(r)}{n_i(0)}\right)^{\left(1-\frac{\mathcal{M}_*^2}{1+\mathcal{M}_*^2}\frac{Z_i e n_i}{p'}\langle U_{1,i\theta}\rangle\right)Z_W/Z_i} \times \times \exp\left\{\frac{\tilde{m}}{m_*}\frac{(3+2\mathcal{M}_*^2)\mathcal{M}_*^4}{(1+\mathcal{M}_*^2)^2}\frac{r}{R_0}\right\}. \quad (41)$$

With the addition of plasma rotation, the augmentation of $\langle U_{1\theta,i}\rangle$ for the helical core leads to the strong peaking near the magnetic axis noticed earlier. In the rotating case, the saturated impurity density peaks near the axis as compared to off-axis in the axisymmetric case with rotation, as the inward pinch is enhanced by the non-zero poloidal flow for the helical core case. As also can be seen in Fig. 13, the peaking density for helical core is much higher with plasma rotation than for the cases without rotation, as expected. There is reasonably good agreement in the peaking density predicted by Eq. 41 and the obtained peaking as can be noticed in Fig. 14.

V. CONCLUSIONS AND FUTURE WORK

In the current work, we have performed simulations of neoclassical transport of trace heavy impurities. We considered ideal MHD equilibria computed with `VMEC` for kinked and unkinked plasmas pertaining to JET-like hybrid scenarios. In order to perform the particle-orbit following, we used the guiding-centre code `VENUS-LEVIS` with added modifications for plasma flow and also include the neoclassical friction force through a Monte-Carlo collision operator. The inward flux from neoclassical friction force depends on the flow velocity of the background ions, and we find that it has a strong dependence on the poloidal velocity $\langle U_{1\theta,i}\rangle$, which depends solely on the magnetic geometry of the equilibrium.

We first benchmarked for an axisymmetric case without rotation and observed that the impurity density peaking does indeed satisfy the theoretically predicted scaling. On doing another axisymmetric case including rotation but without neoclassical effects, we find that the diffusivity increase also follows the predicted scaling from the neoclassical transport of impurity species with rotation. Having established the benchmarking of the tungsten behaviour with and without rotation, we proceed to perform simulations of tungsten transport with realistic account of the parallel flow velocity of the background ions. We find that the parallel velocity of the ions in the core region is much higher in a helical core than in axisymmetry, thus imparting an inward drift to the impurity particles, dragging them towards the axis. For the case of axisymmetry with rotation, the impurity particle densities saturate at the boundary of the core, as expected from neoclassical theory. We find that this is because of the centrifugal effects competing with the neoclassical inward pinch, where the centrifugal effects encourage a strong outward diffusion. For the strong helical core case, the inward flux is strongly enhanced by the augmented poloidal velocity $U_{1\theta,j}$ of the background ions near the magnetic axis, thereby strongly increasing the impurity peaking. This has been shown to occur very quickly (30ms) if the Tungsten Mach number is high, but slowly (2s) is rotation is ignored. We thus conclude that the helical core geometry is key to the dominating inward pinch of impurities with a helical continuous mode in a

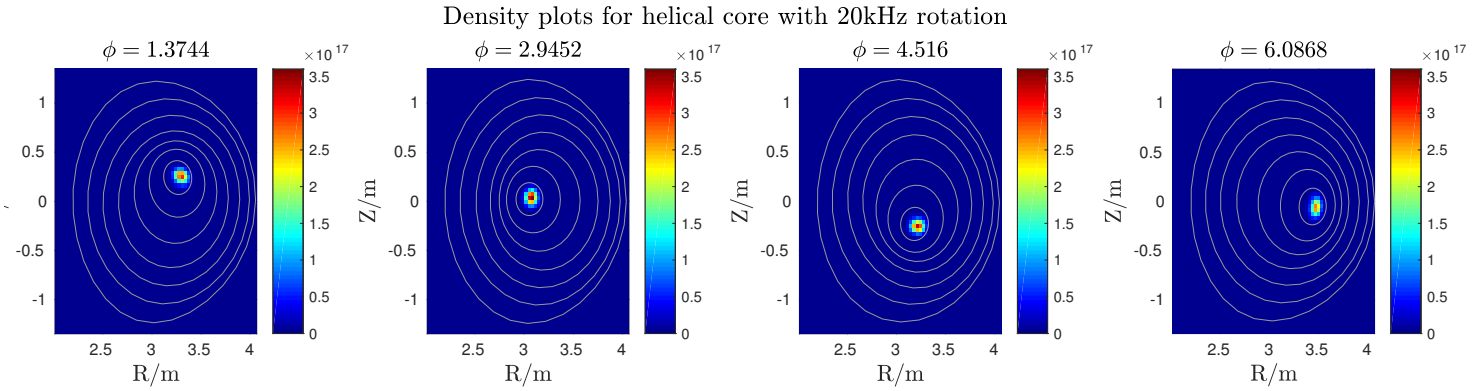

FIG. 12. Plots of density of tungsten on various toroidal cuts for a helical core case with 20kHz rotation, assuming a value of the geometrical factor G_b consistent with the equilibrium. One can notice that the impurities for this case are pinched much closer towards the axis, following the axis of the helical core.

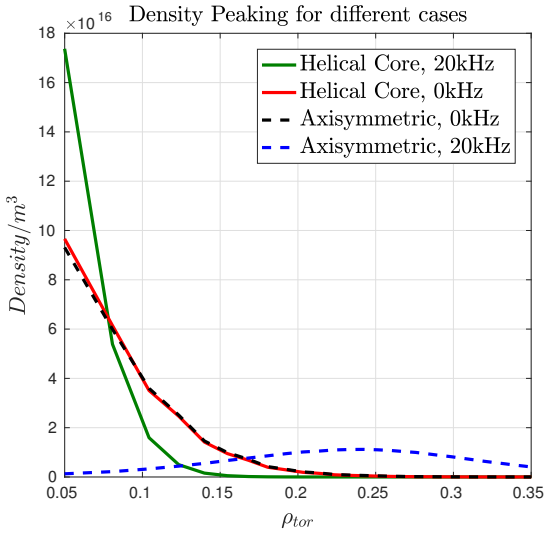

FIG. 13. Plot of intensity of density peaking for axisymmetry and helical core without flow and helical core with flow. The figure is zoomed to $\rho_{tor} = 0.35$ for convenience of comparison.

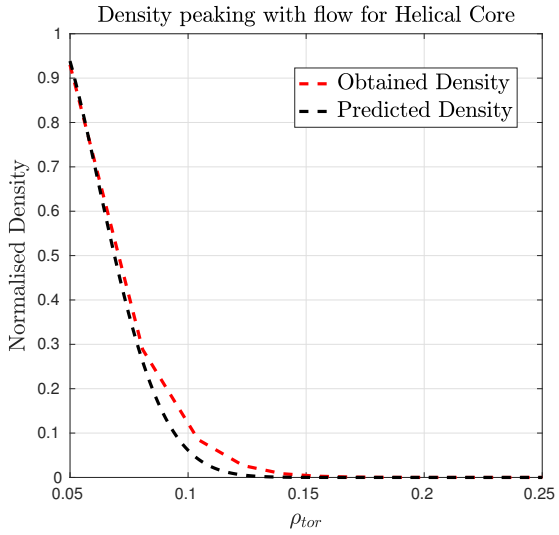

FIG. 14. Comparison of obtained density with density predicted from Eq. 41.

JET-like hybrid operation scenario.

The neoclassical contribution becomes smaller and smaller as the helical core weakens to approach axisymmetry. Thus, by controlling and reducing the strength of the helical core, it is possible for the centrifugal outward advection to compete strongly with the inward neoclassical friction force, pushing the impurities further away from the magnetic axis. And given the larger trapped fractions for the helical core, the centrifugal effects will also be enhanced leading to a more efficient expulsion of impurities away from the magnetic axis. This could be very useful for impurity control in JET hybrid-scenario beam-injected plasmas.

Finally, as we have chosen the most pessimistic case, by not allowing for the temperature screening to occur, the inclusion of a temperature gradient effects on the impurity pinch will be the subject of future work culminating in modelling of realistic JET-like beam-injected hybrid scenario plasmas.

ACKNOWLEDGMENTS

This work has been carried out within the framework of the EUROfusion Consortium and has received funding from the Euratom research and training programme 2014-2018 under grant agreement No. 633053. The views and opinions expressed herein do not necessarily reflect those of the European Commission. The project was also

supported in part by the Swiss National Science Foundation. The authors thank Dr. S. P. Hirshman for providing us with the VMEC equilibrium code.

The current work has involved intense computational resources on multiple clusters. The sections on the computation of the VMEC equilibria and geometrical factor calculations through use of memory intensive TERPSICHORE were supported by EPFL through the use of the computational facilities of the Scientific IT and Application Support Center (EPFL SCITAS). The particle orbit calculations on VENUS-LEVIS were through the Swiss National Supercomputing Center (CSCS, Lugano, Switzerland), through the Helios supercluster (IFERC, Japan), and partially through the Marconi-Fusion cluster in CINECA (Italy).

The first author would also like to especially thank S. Lanthaler for insightful discussions regarding the guiding-center formulation.

Appendix A: Evaluation of drift terms with rotation

In this appendix, we expand the perpendicular particle drifts and provide an explanation as to how the $\mathbf{E}_0 \times \mathbf{B}$ flow term cancels out in the expressions for the particle motion even though we explicitly include Φ_0 in the Hamiltonian. We first evaluate the drifts by expanding the terms in Eq. 25. Now, the value of $\mathbf{E}^* \times \mathbf{b}$ can be given by

$$\mathbf{E}^* \times \mathbf{b} = \left\{ \mathbf{E} - \left(\frac{\mu_j}{Z_j e} + \frac{Z_j e}{m_j} \rho_{\parallel,j}^2 B \right) \nabla B - \frac{1}{2} \frac{m_j}{Z_j e} \nabla (U_{0,j}^2) - \rho_{\parallel,j} \nabla (\mathbf{U}_{0,j}.\mathbf{B}) \right\} \times \mathbf{b}, \tag{A1}$$

which could be written as

$$\mathbf{E}^* \times \mathbf{b} = \left\{ \mathbf{E} - \frac{\mu_j}{Z_j e} \nabla B - \frac{1}{2} \frac{m_j}{Z_j e} \nabla U_{0,j}^{*2} \right\} \times \mathbf{b}, \tag{A2}$$

where we have just substituted $\mathbf{U}_{0,j} + Z_j e \rho_{\parallel,j} \mathbf{B}/m_j = \mathbf{U}_{0,j}^*$. We can now expand

$$\frac{1}{2} \nabla U_{0,j}^{*2} = \nabla \left(\frac{1}{2} \mathbf{U}_{0,j}^*.\mathbf{U}_{0,j}^* \right) = \mathbf{U}_{0,j}^*.\nabla \mathbf{U}_{0,j}^* + \mathbf{U}_{0,j}^* \times (\nabla \times \mathbf{U}_{0,j}^*) \tag{A3}$$

Thus, $\dot{\mathbf{X}}_j$ becomes

$$\dot{\mathbf{X}}_j = (\mathbf{U}_{0,j}^*.\mathbf{b}) \frac{\mathbf{B}^*}{B_\parallel^*} + \frac{1}{B_\parallel^*} \left\{ \mathbf{E} - \frac{\mu_j}{Z_j e} \nabla B - \frac{m_j}{Z_j e} \mathbf{U}_{0,j}^*.\nabla \mathbf{U}_{0,j}^* - \frac{m_j}{Z_j e} \mathbf{U}_{0,j}^* \times (\nabla \times \mathbf{U}_{0,j}^*) \right\} \times \mathbf{b}. \tag{A4}$$

We can now expand $\{\mathbf{U}_{0,j}^* \times (\nabla \times \mathbf{U}_{0,j}^*)\} \times \mathbf{b}$, and take it out of the curly brackets,

$$\{\mathbf{U}_{0,j}^* \times (\nabla \times \mathbf{U}_{0,j}^*)\} \times \mathbf{b} = (\mathbf{U}_{0,j}^*.\mathbf{b}) \nabla \times \mathbf{U}_{0,j}^* - (\nabla \times \mathbf{U}_{0,j}^*.\mathbf{b}) \mathbf{U}_{0,j}^*, \tag{A5}$$

which can then be merged with the first term on the RHS. Realizing that $\mathbf{B}^* = \mathbf{B} + m_j \nabla \times \mathbf{U}_{0,j}^*/Z_j e$, we have now

$$\dot{\mathbf{X}}_j = \frac{\mathbf{U}_{0,j}^*.\mathbf{b}}{B_\parallel^*} \left\{ \mathbf{B} + \frac{m_j}{Z_j e} \nabla \times \mathbf{U}_{0,j}^* \right\} - \frac{m_j}{Z_j e} \frac{\mathbf{U}_{0,j}^*.\mathbf{b}}{B_\parallel^*} \nabla \times \mathbf{U}_{0,j}^* + \frac{m_j}{Z_j e} \frac{\mathbf{U}_{0,j}^*}{B_\parallel^*} \mathbf{b}.\nabla \times \mathbf{U}_{0,j}^* - \frac{\mathbf{b}}{B_\parallel^*} \times \left\{ \mathbf{E} - \frac{\mu_j}{Z_j e} \nabla B - \frac{m_j}{Z_j e} \mathbf{U}_{0,j}^*.\nabla \mathbf{U}_{0,j}^* \right\}. \tag{A6}$$

We can see that a part of the first and the complete second term cancel out. Now, we can obtain $\mathbf{b}.\nabla \times \mathbf{U}_{0,j}^*$ from:

$$B_\parallel^* = B + \frac{m_j}{Z_j e} \mathbf{b}.\nabla \times \mathbf{U}_{0,j}^*, \tag{A7}$$

and on substituting, we get

$$\dot{\mathbf{X}}_j = \mathbf{U}_{0,j}^* - \frac{B}{B_\parallel^*} \{\mathbf{U}_{0,j}^* - (\mathbf{U}_{0,j}^*.\mathbf{b})\mathbf{b}\} - \frac{\mathbf{b}}{B_\parallel^*} \times \left\{ \mathbf{E} - \frac{\mu_j}{Z_j e} \nabla B - \frac{m_j}{Z_j e} \mathbf{U}_{0,j}^*.\nabla \mathbf{U}_{0,j}^* \right\}. \tag{A8}$$

Now, $\mathbf{U}_{0,j}^* - (\mathbf{U}_{0,j}^*.\mathbf{b})\mathbf{b}$ is just $\mathbf{U}_{0\perp,j}^*$ and that $\mathbf{U}_{0\perp,j}^* B = \mathbf{b} \times (\mathbf{U}_{0\perp,j}^* \times \mathbf{B})$. We also substitute the electric field $\mathbf{E} = -\nabla \Phi_0 - \nabla \Phi_1$. Doing so, we now have

$$\dot{\mathbf{X}}_j = \mathbf{U}_{0,j}^* - \frac{\mathbf{b}}{B_\parallel^*} \times (\mathbf{U}_{0\perp,j}^* \times \mathbf{B} - \nabla \Phi_0) + \frac{\mathbf{b}}{B_\parallel^*} \times \left\{ -\nabla \Phi_1 - \frac{\mu_j}{Z_j e} \nabla B - \frac{m_j}{Z_j e} \mathbf{U}_{0,j}^*.\nabla \mathbf{U}_{0,j}^* \right\}. \tag{A9}$$

From ideal Ohm's law, we know that $\mathbf{U}_{0\perp,j}^* \times \mathbf{B} - \nabla \Phi_0 = 0$, thus we have out expression finally reduced to

$$\dot{\mathbf{X}}_j = \mathbf{U}_{0,j}^* + \frac{\mathbf{b}}{B_\parallel^*} \times \left\{ \nabla \Phi_1 + \frac{\mu_j}{Z_j e} \nabla B + \frac{m_j}{Z_j e} \mathbf{U}_{0,j}^*.\nabla \mathbf{U}_{0,j}^* \right\}. \tag{A10}$$

And hence, the higher-order electric field $-\nabla \Phi_0$ has effectively canceled out leading the perpendicular drifts to only depend on the leading-order electric field. From similar calculations, we obtain an expression for $\dot{\rho}_{pa,j}$

$$\dot{\rho}_{\parallel,j} = \frac{\mathbf{B}^*}{\mathbf{B}.\mathbf{B}^*}. \left\{ \nabla \Phi_1 + \frac{\mu_j}{Z_j e} \nabla B + \frac{m_j}{Z_j e} \mathbf{U}_{0,j}^*.\nabla \mathbf{U}_{0,j}^* \right\} \tag{A11}$$

The final expressions for the drifts are the similar to the one obtained in Ref. 18 and Ref. 30.

Appendix B: Calculation of the extra terms in $\mathbf{E}^*$ and $\mathbf{B}^*$ assuming a time-invariant sheared toroidal flow $\Omega(\psi)$

In this section, we describe the expressions for the $\mathbf{B}^* \times \mathbf{E}^*$ drifts implemented in VENUS-LEVIS. To begin with,

we now assume a sheared toroidal flow that only depends on the radial variable ψ, i.e.

$$\Omega \equiv \Omega(\psi) \tag{B1}$$

such that one has a flow that takes the form

$$\mathbf{U}_{0,j} = R^2\Omega\nabla\phi = \Omega\mathbf{e}_\phi. \tag{B2}$$

This approximation simplifies the toroidal flow problem, and is the same treatment of flow used for `SATIRE` equilibrium calculations. In this sense, the particle orbits solved from the guiding-center equations would be consistent with the equilibrium assumed for such calculations.

From the previous section, we have obtained the following redefinitions:

$$\mathbf{A}^* = \mathbf{A} + \rho_{\parallel,j}\mathbf{B} + \frac{m_j}{Z_j e}\mathbf{U}_{0,j}, \tag{B3}$$

$$\mathbf{B}^* = \mathbf{B} + \rho_{\parallel,j}\nabla\times\mathbf{B} + \frac{m_j}{Z_j e}\nabla\times\mathbf{U}_{0,j}, \text{ and} \tag{B4}$$

$$\begin{aligned}\mathbf{E}^* =& \mathbf{E} - \left(\frac{\mu_j}{Z_j e} + w_{\parallel,j}\rho_{\parallel,j}\right)\nabla B - \rho_{\parallel,j}\frac{\partial\mathbf{B}}{\partial t} \\ &- \frac{1}{2}\frac{m_j}{Z_j e}\nabla(U_{0,j}^2) - \rho_{\parallel,j}\nabla(U_{0\parallel,j}B).\end{aligned} \tag{B5}$$

One can see that there are some extra terms in presence of the flow that are not found in the flow-free stationary frame guiding-center equations. Using the form for the flow above, we now proceed to compute those terms. The term $\nabla\times\mathbf{U_0}$ is given by

$$\begin{aligned}\nabla\times\mathbf{U}_{0,j} &= \nabla\times(R^2\Omega\nabla\phi) \\ &= -\frac{R^2\Omega}{\sqrt{g}}\left(\frac{1}{\Omega}\frac{\partial\Omega}{\partial\psi} + \frac{2}{R}\frac{\partial R}{\partial\psi}\right)\mathbf{e}_\theta + \frac{2R\Omega}{\sqrt{g}}\frac{\partial R}{\partial\theta}\mathbf{e}_\psi.\end{aligned} \tag{B6}$$

This expression gives the $\nabla\times\mathbf{U_0}$ in the contravariant form and, if needed, the covariant form can be obtained by vector multiplication with the contravariant metric g^{ij}. Now, $|\mathbf{U_0}| = R\Omega$, therefore, we can calculate ∇U_0^2 to be

$$\begin{aligned}\nabla U_{0,j}^2 &= \nabla R^2\Omega^2 \\ &= 2R^2\Omega^2\left[\left(\frac{1}{\Omega}\frac{\partial\Omega}{\partial\psi} + \frac{1}{R}\frac{\partial R}{\partial\psi}\right)\nabla\psi + \frac{1}{R}\frac{\partial R}{\partial\theta}\nabla\theta\right].\end{aligned} \tag{B7}$$

Now, the term $\nabla U_{0\parallel,j}B$ can be written as $\nabla(\mathbf{U}_{0,j}.\mathbf{B})$ which can be written as

$$\begin{aligned}\nabla(\mathbf{U}_{0,j}.\mathbf{B}) &= \nabla(\Omega R^2\nabla\phi.\mathbf{B}) = \nabla\Omega R^2 B^\phi \\ &= R^2B^\phi\frac{\partial\Omega}{\partial\psi}\nabla\psi + 2\Omega RB^\phi\left(\frac{\partial R}{\partial\psi}\nabla\psi + \frac{\partial R}{\partial\theta}\nabla\theta\right) \\ &+ \Omega R^2\nabla B^\phi.\end{aligned} \tag{B8}$$

Now with all the terms present, we may implement the new corresponding guiding center equations. Again, these drifts have a form equivalent to Sec. III-C of Ref. 18.

Appendix C: Quasi-neutrality corrections in case of plasma rotation

One way to calculate this compensating potential and its corresponding field is to assume a local Maxwellian for the ion and electron species of the plasma and manually minimize the charge separation. Now, the electric field at equilibrium, is split into its zeroth order and first order potentials[52]

$$\mathbf{E} = -\nabla\Phi_0 - \nabla\Phi_1 \tag{C1}$$

where the leading order field is caused by the rotation of the plasma, and the first-order correction is necessary for preserving quasi-neutrality.

In order to transform the energy in the rotating frame in terms of quantities in the stationary frame, we express the thermal velocities with respect to their lab frame counterparts. Thus, we apply:

$$w_{\parallel,j} = v_{\parallel,j} - U_{0\parallel,j}, \mathbf{w}_{\perp,j} = \mathbf{v}_{\perp,j} - \mathbf{U}_{0\perp,j}, \tag{C2}$$

where $\mathbf{U}_{0\parallel,j}$ and $\mathbf{U}_{0\perp,j}$ are the parallel and perpendicular flow velocities of the plasma. Single particles of species j in the rotating frame have the energy

$$E_{rot,j} = \frac{1}{2}m_j w_{\parallel,j}^2 + \mu_j B - \frac{1}{2}m_j\Omega^2R^2 + Z_j e\Phi_1. \tag{C3}$$

Here, $w_{\parallel,j}$ refers to the thermal fluctuation component of the parallel velocity of the particle of species j. Also, the magnetic moment of the thermal part of the gyromotion $\mu_j = m_j w_{\perp,j}^2/2B$, where $w_{\perp,j}$ is the thermal component of the perpendicular velocity of the particle, and which should not be confused with the magnetic moment in lab frame. The third term is the energy contribution of the centrifugal force. Φ_1 refers to the higher-order correction in the electric potential. Only this lower order correction to the electric potential is observed by the particles in the rotating frame.

The particle distribution can now be locally expressed as the Maxwellian by integrating over the velocities $w_{\parallel,j}$ and $w_{\perp,j}$

$$F_j(\psi) = \frac{\bar{n}_j(\psi)}{[2\pi T_j(\psi)]^{3/2}}\exp\left(-\frac{E_{rot}}{T_j(\psi)}\right). \tag{C4}$$

Integrating for the number density $n_j(\psi,\theta)$, one can derive the relation

$$n_j(\psi,\theta) = \bar{n}_j(\psi)\exp\left(\frac{m_j\Omega^2R^2}{2T_j} - \frac{Z_j e\Phi_1}{T_j}\right). \tag{C5}$$

Onn preserving the quasi-neutrality between ions and electrons (subscripts i and e respectively) through

$$\sum_{j=\{i,e\}} n_j(\psi,\theta)Z_j e = 0, \tag{C6}$$

and we obtain Φ_1 as

$$\Phi_1(\psi,\theta) = \frac{m_i\Omega^2R^2}{2e}\frac{T_e}{T_i+T_e}. \tag{C7}$$

If we assume that both the ions and the electrons have the same temperature, one can see that the potential Φ_1 is half the value in magnitude to the energy contributed by the centrifugal term. This term for ions reduces some of the displacement caused by the rotation by a factor of $\mathcal{M}^2_{*,i}$, and for electrons increases it by the same factor $\mathcal{M}^2_{*,e}$. The densities for species j then becomes

$$n_j(\psi,\theta) = \bar{n}_j(\psi)\exp\mathcal{M}^2_{*,j}, \tag{C8}$$

where $\mathcal{M}^2_{*,j}$ is

$$\mathcal{M}^2_{*,j} = \left(m_j - \frac{m_i T_e}{T_i + T_e}\right)\frac{\Omega^2 R^2}{2T_j} \tag{C9}$$

In doing so, it brings the ions and electrons densities closer. Therefore, one can see that the effect of the centrifugal force trying to violate the quasi-neutrality is mitigated by the lower-order potential. So far, these calculations are valid only for axisymmetric equilibria.

[1]Pütterich T., Neu R., Dux R., Whiteford A. D., O'Mullane M. G., Summers H. P. and the ASDEX- Upgrade Team. Nuclear Fusion **50**, 025012 (2010).
[2]Sertoli, M. et al, Nuclear Fusion **55**, 113029 (2015).
[3]Anh J.-H., Garbet, X., Luetjens, H. and Guirlet, R.. Submitted to PPCF (2016).
[4]Casson F.J. et al, Plasma Phys. Control. Fusion 57, 014031 (2015).
[5]Sertoli M. et al, Plasma Phys. Control. Fusion 57, 075004 (2015).
[6]Hender, T.C. et al, Nucl. Fusion **56**, 066002 (2016).
[7]Wong, K. L., Cheng, C. Z., Phys. Fluids **3**, 545 (1989).
[8]Fülöp, T. and Helander P. Phys. Plasmas 6, 3066 (1999).
[9]Romanelli, M. et al, Plasma Physics and Controlled Fusion **53**, 054017 (2011).
[10]Romanelli, M. and Ottaviani, M. , Phys. Plasma Control. Fusion 40, 1767 (1998).
[11]McKay, R.J. et al, Plasma Phys. Control. Fusion 50, 065017 (2008).
[12]McClements K.G. and McKay R.J., Phys. Plasma Control Fusion 51, 115009 (2009)
[13]Romanelli, M. et al, Plasma Phys. Control. Fusion 53, 054017 (2011).
[14]I. T. Chapman, M. D. Hua, S. D. Pinches, R. J. Akers, A. R. Field, J. P. Graves, R. J. Hastie, C. A. Michael, and The MAST Team, *Nuclear Fusion* **50**, 045007 (2010).
[15]I. T. Chapman, D. Brunetti, P. Buratti, W. A. Cooper, J. P. Graves, J. R. Harrison, J. Holgatem S. Jardin, S. A. Sabbagh, K. Tritz, the MAST and NSTX Teams and EFDA-JET Contributors, *Nuclear Fusion* **54**, 083007 (2014).
[16]Pfefferlé, D. et al., NBI fast ion confinement in the helical core of MAST hybrid-like plasmas. Nucl. Fusion **54** 064020 (2014).
[17]Boozer, A. H. , Physics of Fluids **24**, 1999 (1981).
[18]Brizard, A.J., Phys. Plasmas 2, 459 (1995).
[19]S. P. Hirshman, *Physics of Fluids* **26**, 3553 (1983).
[20]S. P. Hirshman, W. I. van Rij, and P. Merkel, *Computer Physics Communications* **43**, 143 (1986).
[21]W. A. Cooper, J. P. Graves, A. Pochelon, O. Sauter, and L. Villard, *Physical Review Letters* **105**, 035003 (2010).
[22]D. Pfefferlé, W. A. Cooper, J.P. Graves, and C. Misev, *Computer Physics Communications* **185**, 3127 (2014).
[23]K.C.Shaing, K. Ida, and S.A. Sabbagh, Nuclear Fusion 55, 125001, (2015)
[24]Nakajima, N. and Okamoto, *Journal of the Physical Society of Japan* **61**, 833 (1992).
[25]Helander, P. and Sigmar, D.J., Collisional Transport in Magnetized Plasmas (2005).
[26]Helander, P., Rep. Prog. Phys. **77**, 087001 (2014).
[27]Helander, P., Phys. Rev. Lett. **118**, 155002 (2017).
[28]J. Wesson, *Tokamaks, 4th Ed.*, Sec. 3.11, 123-125 (2011).
[29]Angioni C. and Helander P., Plasma Phys. Control. Fusion 56, 124001 (2014).
[30]Peeters, A. G. et al., *Physics of Plasmas* **16**, 042310 (2009).
[31]D. Brunetti, J. P. Graves, W. A. Cooper and D. Terranova, *Nuclear Fusion* **54**, 064017 (2014)
[32]K. Shaing and J. Callen, *Physics of Fluids* **26**, 3315 (1983).
[33]K. Shaing, S. .P. Hirshman, and J. Callen, *Physics of Fluids* **29**, 521 (1986).
[34]Romanelli, M. *Study of high-Z impurity accumulation and transport in the JET Tokamak plasmas from soft X-ray tomography.* PhD thesis, University of London, Imperial College of Science, Technology and Medicine (1998).
[35]Huba, J. NRL Plasma Formulary.
[36]Ware, A.A., Phys. Rev. Lett. **25**, 15-17 (1970).
[37]A. D. Turnbull, W. A. Cooper, L. L. Lao, and L.-P. Ku, *Nuclear Fusion 51*, 123011 (2011).
[38]W. A. Cooper, S .F. I. Margalet, S. J. Allfrey, J. Kisslinger, H. F. G. Wobig, Y. Narushima, S. Okamura, C. Suzuki, K. Y. Watanabe, K. Yamazaki, and M. Yu. Isaev, *Fusion Science and Technology* **46**, 365 (2004).
[39]M. Raghunathan et al, *Nuclear Fusion* **56**, 092004 (2016).
[40]Graves, J. P., Hastie, R. J. and Hopcraft, K. I., Effects of sheared toroidal plasma rotation on the internal kink mode in the banana regime. Plasma Phys. Control. Fusion **42**, 1049 (2000).
[41]Cary, J. R. and Brizard, A. J., Hamiltonian theory of guiding-center motion. Rev. Mod. Phys. **81**, 693 (2009)
[42]Cooper, W. A. et al., An approximate single fluid 3-dimensional magnetohydrodynamic equilibrium model with toroidal flow. Plasma Phys. Control. Fusion **56**(9) 094004 (2014).
[43]Cooper, W. A. et al., Free boundary equilibrium in 3D tokamaks with toroidal rotation. Nuclear Fusion **55** 063032 (2015).
[44]Littlejohn, R. G., Variational principles of guiding-centre motion. J. Plasma Physics **29**(1), 111 (1983)
[45]K. Y. Watanabe, N. Nakajima, M. Okamoto, K. Yamazaki, Y. Nakamura, and M. Wakatani, *Nuclear Fusion* **35**, 335 (1995).
[46]M. Yu. Isaev, W. A. Cooper, K. Y. Watanabe, and N. Nakajima, *Proceedings of the 30th Conference on Controlled Fusion and Plasma Physics* **27**, 4, (2003).
[47]A. Wingen, N. M. Ferraro, M. W. Shafer, E. A. Unterberg, J. M. Canik, T. E. Evans, D. L. Hillis, S. P. Hirshman, S. K. Seal, P. B. Snyder, and A. C. Sontag, *Plasma Physics and Controlled Fusion* **57**, 104006 (2015).
[48]W. A. Cooper, *Plasma Physics and Controlled Fusion* **34**, 1011 (1992).
[49]K. Y. Watanabe, N. Nakajima, M. Okamoto, Y. Nakamura, and M. Wakatani, *Nuclear Fusion* **32**, 1499 (1992).
[50]J. L. Johnson, K. Ichiguchi, Y. Nakamura, M. Okamoto, M. Wakatani, and N. Nakajima, *Physics of Plasmas* **6**, 2513 (1999).
[51]D. V. Anderson, W. A. Cooper, R. Gruber, S. Merazzi, and U. Schwenn, *International Journal of High Performance Computing Applications* **1**, 34 (1990).
[52]Hinton, F. L. and Hazeltine, R. D., Rev. Mod. Phys. **48**, 239 (1976).